Bond Characteristic-Dependent Viscosity Variations in CaF_2-SiO_2-Al_2O_3-MgO Welding Fluxes

The effect of oxygen/fluorine-related bond characteristics on the viscosity of CaF_2–SiO_2–Al_2O_3–MgO submerged arc welding fluxes is evaluated

BY H. YUAN, Y. ZHANG, H. LIU, Z. LI, AND C. WANG

Abstract

Viscosity is critical in welding fluxes as it could affect weldability and alloying element transfer behaviors during submerged arc welding. It is widely accepted that viscosity is intrinsic to bonding structures. However, it is unclear how such structures could modify viscosity in commercial CaF_2-SiO_2-Al_2O_3-MgO fluxes. In this study, structure-viscosity correlations have been revealed by employing molecular dynamics calculations coupled with viscosity measurements. The results show that viscosity at 1300°C reaches maximum (1.99 Pa·s) and minimum values (0.10 Pa·s) at the highest SiO_2 and MgO levels, respectively. Furthermore, bond stability and distribution could indicate the structural degree of polymerization. Specifically, the proportion of stabilized bridging oxygen and bonded F (Si-F and Al-F) correlates positively with the activation energy of viscous flow. Due to the dilution effect of free F and the depolymerization effect of bonded F, the activation energy of viscous flow in the targeted system (60–130 kJ/mol) is significantly lower than in fluorine-free ones (160–240 kJ/mol). The current investigation establishes a relationship between bond stability and viscous flow activation energy, demonstrating a stronger correlation than considering O-related structural parameters alone.

Keywords

- Welding Flux
- Viscosity
- Bond Characteristic
- Molecular Dynamics
- Structure

Introduction

High heat input submerged arc welding (SAW) is one of the most popular techniques for joining oil and gas pipelines and shipbuilding steels (Refs. 1–3). However, successfully demonstrating such a technique relies heavily on selecting suitable welding fluxes (Ref. 4). Commercial fluxes such as those based on CaF_2-SiO_2-Al_2O_3-MgO possess necessary physicochemical properties in protecting the weld pool from the atmosphere, refining the weld metal (WM) via element transfer, and minimizing heat loss through thermal insulation (Refs. 1, 5, 6).

Viscosity is one of the most important properties of welding fluxes. It could dictate mass and heat transport, significantly affecting weld bead morphology and alloying elements transfer behaviors between the slag and the WM (Refs. 7, 8). Schwemmer et al. (Ref. 8) reported that weld bead penetration increased with flux viscosity. Specifically, high viscosity will prevent the weld pool from spreading, reducing the heat region and resulting in deeper penetration and narrower bead width (Refs. 8, 9). Furthermore, low viscosity will facilitate bulk diffusion rates and accelerate the reaction rates at the metal-slag interface (Refs. 8, 9). Thus, accurately quantifying and controlling viscosity is crucial for achieving desirable weld metal morphology and composition. However, viscosity could fluctuate at varied temperatures and compositions (Refs. 10, 11). Such property is linked to the atomic structure of molten fluxes and is governed by internal

https://doi.org/10.29391/2025.104.009

structural characteristics (Refs. 12–14). Hence, numerous experimental and simulation efforts have sought to determine the relationship between viscosity and assorted structural parameters (Ref. 15). One commonly used structural parameter for describing the degree of polymerization (DOP) is NBO/T, which represents the average number of nonbridging oxygen per network former (Si^{4+}, Al^{3+}) (Refs. 10, 16). Some researchers prefer using the parameter Qi (i ranges from 0 to 4, and i represents the number of bridging oxygens in one [SiO_4] or [AlO_4] tetrahedra) (Ref. 16). Both parameters can reflect the DOP of fluxes but fail to differentiate the effects of different cations on structural properties. In response, Zhang et al. (Ref. 17) pioneered a structural viscosity model, defining distinct categories of oxygen ions and assigning varying priorities to different metal cations in compensating Al^{3+} ions. Recently, He et al. (Ref. 12) introduced a viscosity model pertinent to the SiO_2-CaO-K_2O biomass slag system based on bond distribution, which is associated with the activation energy of viscous flow. Nevertheless, the bond distributions were approximations from the thermodynamic equilibrium

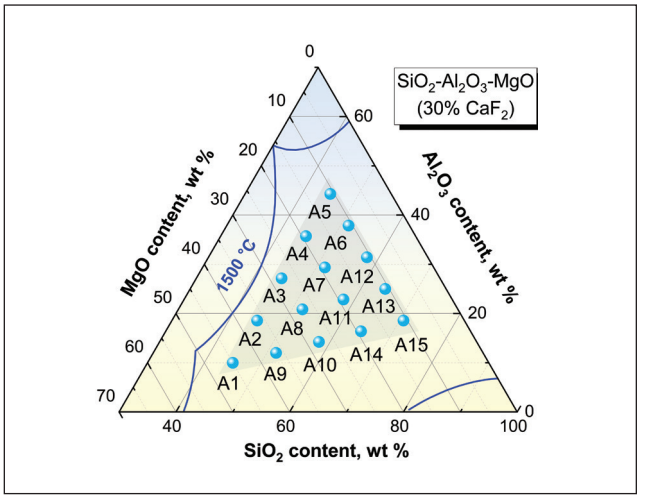

Fig. 1 — Chemical compositions of the welding fluxes (total mass fraction of SiO_2, Al_2O_3, and MgO have been converted to 100% in the diagram).

Table 1 — Chemical Compositions (wt-%) of the Welding Fluxes

No.	Component							
	SiO_2		Al_2O_3		MgO		CaF_2	
	Pre	Post	Pre	Post	Pre	Post	Pre	Post
A1	31.5	32.10	7.00	7.17	31.5	31.65	30.0	29.08
A2	31.5	32.12	13.0	12.75	25.5	25.34	30.0	29.79
A3	31.5	32.08	19.0	18.31	19.5	19.63	30.0	29.98
A4	31.5	31.79	25.0	23.99	13.5	15.04	30.0	29.18
A5	31.5	31.74	31.0	30.20	7.50	8.18	30.0	29.88
A6	36.0	36.13	26.5	26.18	7.50	8.14	30.0	29.55
A7	36.0	35.22	20.5	19.9	13.5	15.2	30.0	29.68
A8	36.0	36.43	14.5	14.9	19.5	18.9	30.0	29.77
A9	36.0	36.11	8.50	8.43	25.5	26.6	30.0	28.86
A10	40.5	40.47	10.0	9.76	19.5	21.5	30.0	28.27
A11	40.5	40.51	16.0	16.22	13.5	13.72	30.0	29.55
A12	40.5	41.05	22.0	22.11	7.50	7.76	30.0	29.08
A13	45.0	45.52	17.5	17.28	7.50	7.99	30.0	29.21
A14	45.0	44.76	11.5	11.90	13.5	13.81	30.0	29.53
A15	49.5	49.89	13.0	13.61	7.50	7.44	30.0	29.06

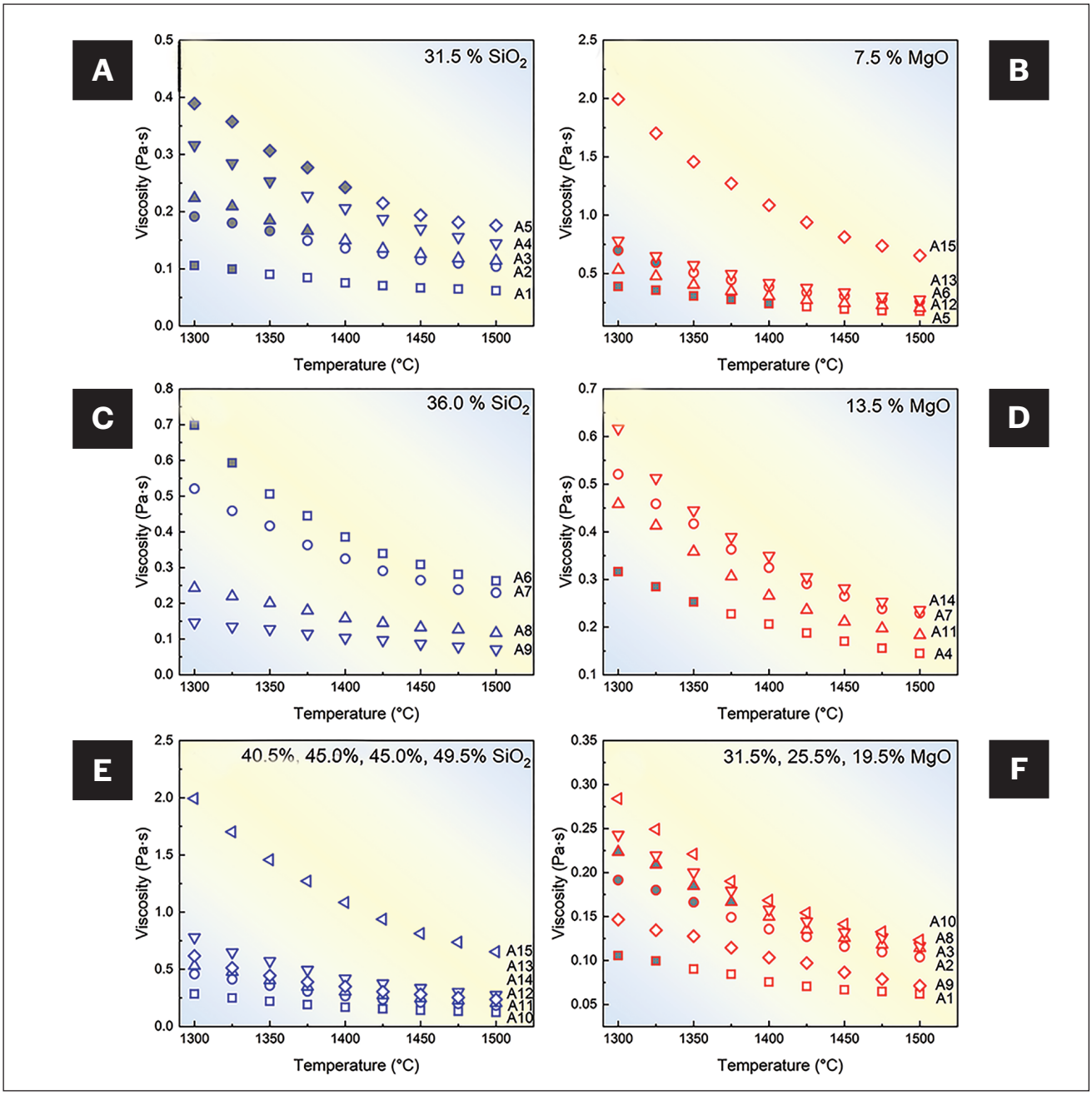

Fig. 2 — Viscosity values of fluxes: A — 31.5% SiO_2; B — 36.0% SiO_2; C — 40.5%, 45.0%, 49.5% SiO_2; D — 7.5% MgO; E — 13.5% MgO; F — 31.5%, 25.5%, 19.5% MgO, where the points in dark grey are lower than the liquidus temperatures calculated by the FactSage software.

state within the FactSage database. Based on the DOP and bond energy, Xuan et al. (Ref. 13) advanced the structural parameter relative stability (RS), offering insight into the network stability of silicate slag melts through molecular dynamics (MD) simulations. Such a method has the advantage of quantifying the influence of all bonds and can differentiate the contributions of oxygen-related bonds from an atomic scale (Ref. 6). These models cater to industrial and geological applications composed of oxide components. In typical welding flux systems, CaF_2 is widely applied as it can efficiently decrease O chemical potential and modify flux viscosity while significantly complicating the structural bonding features of oxide systems (Refs. 7, 18–20). However, the extent to which F-related bonds contribute to flux viscosity quantitatively remains poorly understood, preventing the tuning of viscosity for targeted fluxes. Consequently, a comprehensive understanding of the atomic structures of the CaF_2-based fluxes holds significance for viscosity adjustments and reveals how CaF_2 influences oxide system structures.

In this work, viscosity trials and MD simulations have established a relationship between the viscosity and bond characteristics of CaF_2-SiO_2-Al_2O_3-MgO fluxes. Structural roles of O and F-related species and the corresponding distributions in the targeted system have been elucidated.

Current findings may facilitate a fundamental understanding of bond-induced viscous behaviors and offer a viable strategy to design flux viscosity from an intrinsic structural perspective.

Research Methodology

Sample Preparation

Reagent grade (> 99.9%) chemicals of SiO_2, CaF_2, MgO, and Al_2O_3 (Sinopharm Chemical Reagent Co. Ltd., Shenyang, China) were used for synthesizing the fluxes. The powders were mixed and placed into a molybdenum crucible. The mixed powder samples were pre-melted in a silicon-molybdenum resistance furnace under a high-purity argon atmosphere by holding the sample at 1500°C for 30 min. Afterward, the liquid fluxes were immediately quenched into cold water. Quenched samples were dried at 150°C for 4 h to remove any moisture and subsequently crushed for 30 min. The resulting powders were further sieved to obtain particle size < 74 µm. X-ray fluorescence determined the fluxes' compositions (XRF, ZSX Primus IV, Rigaku, Japan). Chemical compositions of the targeted fluxes are shown in Table 1 and Fig. 1. Slag liquidus temperatures (T_{liq}) were calculated using the FactSage software (Equilib-module, Version 8.1 with FactPS and FToxid databases).

Viscosity Measurements

Viscosity was measured using the rotary cylinder method according to the YB/T 185-2017 standard. The experimental apparatus for viscosity measurement consisted of a $MoSi_2$ resistance heating vertical tube furnace and a melt physical property comprehensive testing instrument (VDR-16000, Chongqing University, China) equipped with a Brookfield digital viscometer (mold DV2T, Brookfield Engineering Laboratories, USA). Before the viscosity test, the viscometer was calibrated with standard silicone oils (0.0967 Pa·s) at 25°C. The experimental procedure for viscosity measurement was described as follows. First, the molybdenum crucible containing 150 g of flux was placed in the uniform temperature zone of the vertical resistance furnace, which was calibrated using a reference B-type thermocouple and controlled within ± 2°C. To protect the molybdenum crucible (Φ48 × H100 mm) from oxidation, high-purity Ar gas flow (99.999 vol-%, 0.7 L/min) was injected from the bottom of an alumina tube. The furnace was then heated to 1600°C and maintained for 15 min to ensure homogeneity. Subsequently, a molybdenum spindle (Φ15 mm × H20 mm; taper degree: 120 deg; shaft diameter: 3 mm) was slowly sunk into the molten fluxes and kept at 15 mm above the crucible bottom. Flux viscosity was measured in the temperature range of 1500° to 1300°C at 25°C intervals after being held at each temperature for 15 min to ensure thermal equilibrium. The viscosity values at the target temperature were the average results obtained at three rotation speeds (10, 20, and 30 rpm), and the deviation of all measured experimental data from the average value is less than 3%.

Table 2 — BMH Function Parameters

Atom 1	Atom 2	A_{ij} (eV)	ρ_{ij} (Å)	C_{ij} (eV·Å^6)
Ca	Ca	329193.3	0.16	4.3369
Ca	Mg	67720.91	0.16	0.8674
Ca	F	496191.6	0.165	8.67
Ca	O	717827	0.165	8.6737
Ca	Si	26686.16	0.16	0
Ca	Al	36934.4	0.16	0
Mg	Mg	13931.4	0.16	0.1735
Mg	F	107066.695	0.165	1.7347
Mg	O	154984.64	0.165	1.7347
Mg	Si	5489.82	0.16	0
Mg	Al	7594.81	0.16	0
F	F	730722.8	0.17	17.35
F	O	1046135	0.17	17.35
F	Si	43406	0.165	0
F	Al	59486.5	0.165	0
O	O	1497693.51	0.17	17.35
O	Si	62821.41	0.165	0
O	Al	86094.6	0.165	0
Si	Si	2163.32	0.16	0
Si	Al	2994.1	0.16	0
Al	Al	4143.9	0.16	0

Molecular Dynamic Simulations

Simulation Method

Molecular dynamics simulations were conducted using the LAMMPS package (Ref. 21). Software PACKMOL (Version 20.3.0) was used to obtain different random initial configurations of the targeted system (Ref. 22). Approximately 4,000 atoms were subjected to a simulated melt-quench process within a cubic box, the size of which was dictated by flux density. Interaction between atoms was characterized by

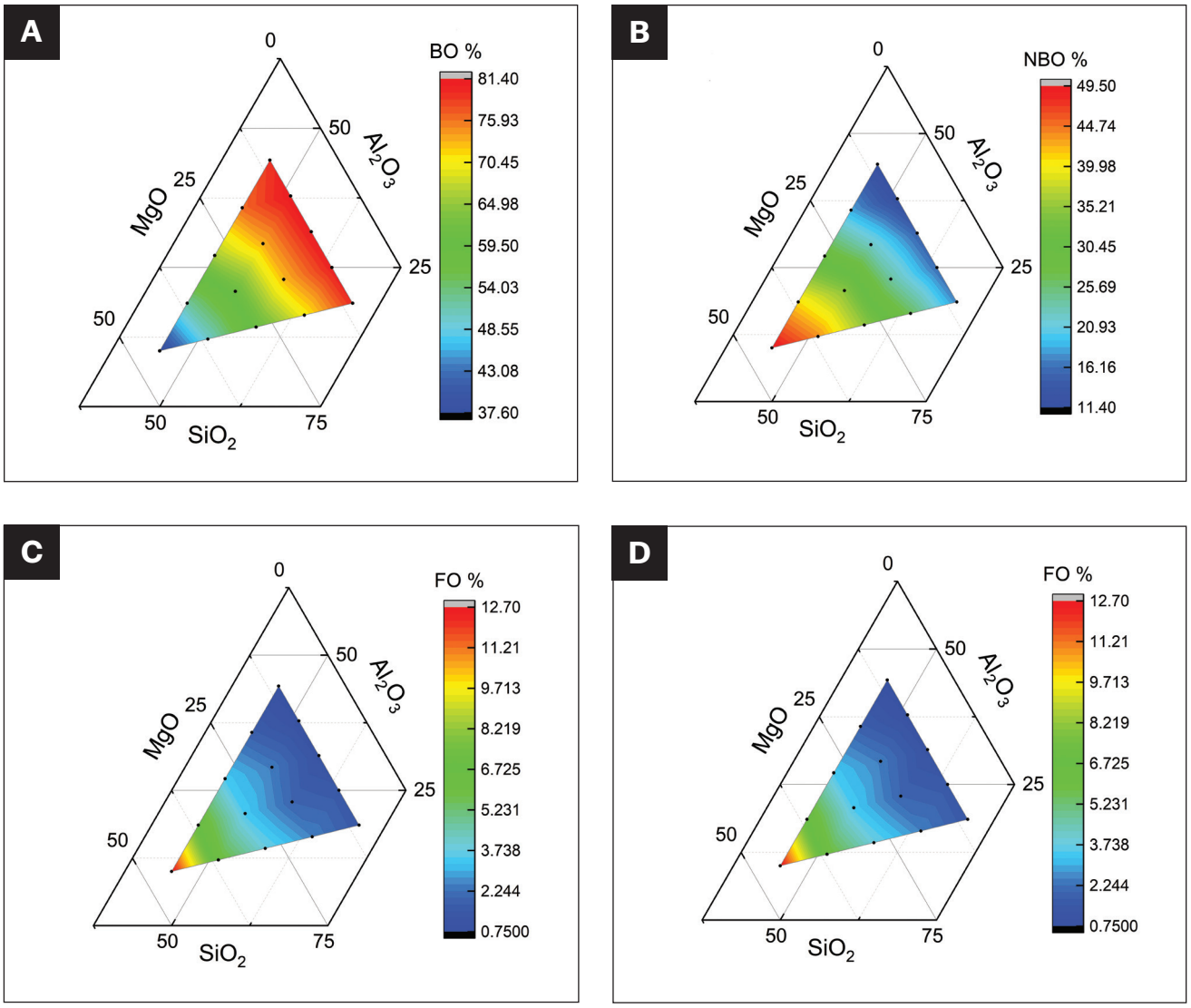

Fig. 3 — Proportions of: A — Bridging oxygen (BO); B — nonbridging oxygen (NBO); C — free oxygen (FO); D — oxygen triclusters (TO) at 1500°C.

Born-Mayer-Huggins (BMH) interatomic potential. The BMH function is expressed as follows:

$$U_{ij}(r) = \frac{Cq_iq_j}{\varepsilon r_{ij}} + A_{ij}e^{-\frac{r_{ij}}{\rho_{ij}}} - \frac{C_{ij}}{r_{ij}^6} + \frac{D}{r^8} \quad (1)$$

In Equation 1, U_{ij} is the interatomic-pair potential. C is an energy-conversion constant. q_i and q_j are the charges for different ions, ε is the dielectric constant, and r_{ij} is the interatomic distance between i atom and j atom. ρ_{ij} is an ionic-pair-dependent length parameter. A_{ij}, C_{ij}, and D are energy parameters of the atom ij pair. BMH function parameters, which have been proven valid through considerable trials (Refs. 23–25), are provided in Table 2. The bond distance was calculated and compared with the experimental values to verify the MD simulations. This parameter was derived from the abscissa of the major peak of the radial distribution functions (RDF) curves. Detailed simulation information can be found elsewhere (Ref. 6).

Diffusion Coefficient Calculation

To calculate the transport properties of the flux systems, the mean square displacement (MSD) curves of each atom are obtained using the following formula:

$$MSD = \langle |r(t) - r(0)|^2 \rangle \quad (2)$$

In this equation, $r(t)$ represents the location of an atom at time t, and $r(0)$ means the starting location of this atom. Then, based on the Einstein's Equation, self-diffusion coefficients for varied atoms are calculated as:

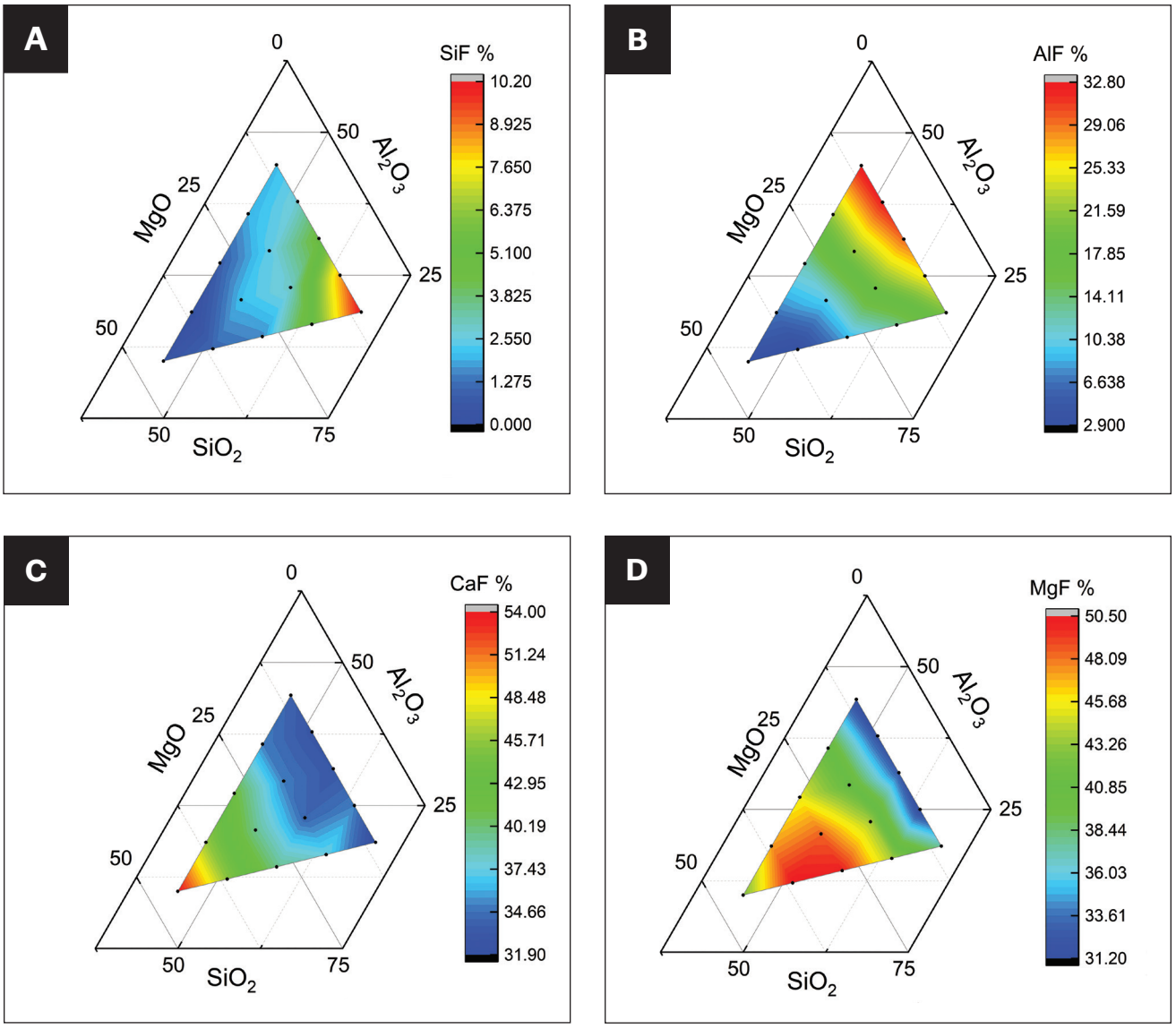

Fig. 4 — Proportions of: A — F-Si; B — F-Al; C — F-Ca; D — F-Mg bonds at 1500°C.

$$D(\mathrm{t}) = \frac{MSD}{6t} \quad (3)$$

where D(t) is the diffusion coefficient.

Bond and Energy Calculation

Oxygen and fluorine species distributions were calculated using MATLAB based on the output trajectory profiles from MD simulations. The last frame of trajectory, consisting of involved atom coordinates, was extracted. Specifically, the first step was to assess whether the bond could be formed. This was determined by comparing the cut-off distance (Rc) with the calculated bond distance. Rc was determined from RDF curves based on the trajectory file. The bond was considered successful if the calculated bond distance was shorter than Rc. Then, the bonding features of the oxygen atoms can be revealed by performing the loop statements in the MATLAB code. Atom energy data were the sum of potential and kinetic energy extracted from the last 0.5 ns period of the simulation.

Results

Viscous Behavior Evaluation

Figures 2A–C illustrate the measured viscosity variation for fixed SiO_2 contents of 31.5%; 36.0%; and 40%, 45.0%, 49.5%, respectively. It is observed that viscosity values increase as expected with higher SiO_2 content. Specifically, at 1300°C, viscosity values escalate from 0.39 Pa·s (A5) to 0.70 Pa·s (A6) and further to 1.99 Pa·s (A15). Higher Al_2O_3/MgO ratios induce a monotonically increasing trend in viscosity (A1→A5, A9→A6, A10→A12, and A14→A13).

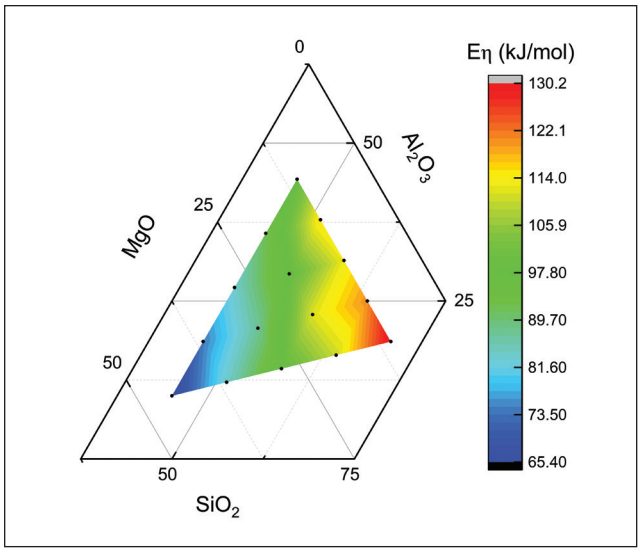

Fig. 5 — Contour lines of activation energy for viscous flow (E_η).

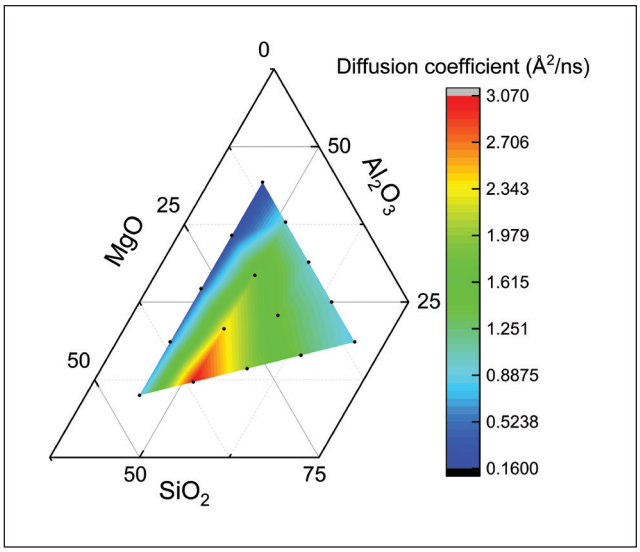

Fig. 6 — Total self-diffusion coefficient values for targeted fluxes.

Table 3 — Comparison of Bond Distances from MD with Experimental Values

Pair	Bond Distance from RDF (Å, this work)	Experimental Data (Å, references)
Si-O	1.62	1.61–1.64 [Refs. 26–28]
Al-O	1.75	1.74–1.77 [Refs. 26–28]
Mg-O	1.99	~ 2.00 [Ref. 29]
Ca-O	2.32	2.32 [Refs. 26, 28]
Si-F	1.68	1.67 [Ref. 29]
Al-F	1.94	1.81–1.92 [Ref. 30]
Ca-F	2.32	2.29 [Ref. 31]
Mg-F	2.05	2.0 [Ref. 31]

Figures 2D–F plot the viscosity values for fixed MgO contents of 7.5%; 13.5%; and 31.5%, 25.5%, 19.5%, respectively. MgO significantly reduces the flux viscosity, as expected. However, viscosity variations induced by different Al_2O_3/SiO_2 ratios could entail intricate ramifications. An increase in the Al_2O_3/SiO_2 ratio primarily tends to reduce the viscosity of most fluxes. Nevertheless, the viscosity values of A11 and A12, with higher SiO_2 contents, are lower than those of A7 and A6, respectively.

MD Verification

Table 3 provides the calculated bond length and the corresponding experimental value for various bond pairs. It can be observed that the average bond lengths of Si-O, Al-O, Mg-O, Ca-O, Si-F, Al-F, Ca-F, and Mg-F are around 1.62Å, 1.75Å, 1.99Å, 2.32Å, 1.68Å, 1.94Å, 2.32Å, 2.05Å, respectively. It gives an excellent agreement between the calculated results and the experimental values (Refs. 26–31). Thus, the present calculations can reproduce a short-range structure in reasonable agreement with the experimental data.

Medium Range Structure

The type and distribution of bonds could dictate viscosity values. Oxygen bonds are classified into four categories based on connectivity: bridging oxygen (BO), nonbridging oxygen (NBO), free oxygen (FO), and oxygen tricluster (TO), where TO serves as charge compensators in aluminosilicates (Ref. 23). Such distribution calculated by MD simulations is shown in Fig. 3. It can be observed that the TO content is the highest in Al_2O_3-rich compositions (A5). As the concentration of network formers (Al_2O_3 and SiO_2) increases, a higher Al coordination is required to balance the overall charge. Moreover, BO bonds are mostly concentrated in Al_2O_3-rich compositions (A5) while least in MgO-rich regions (A1). The color shifts from red to blue with increasing MgO content, while NBO and FO show the opposite trend.

Figure 4 presents F-related bond distributions. In most cases, Si hardly connects with F, followed by Al (Figs. 4A and B). Si-F bonds are found in SiO_2-rich compositions (A12-A15) (Fig. 4A), while other compositions show Si-F bond proportions below 2%. Conversely, Al-F bonds range from 2.9% to 32.8%, with higher concentrations observed in Al_2O_3-rich compositions (A5, A6, and A12), peaking at A5 (Fig. 4B). Fig. 4C shows that Ca-F bonds exhibit the highest proportions (31.9–54.0%), suggesting that F tends to bond with Ca to form CaF_2 clusters, thereby diluting the O-related network.

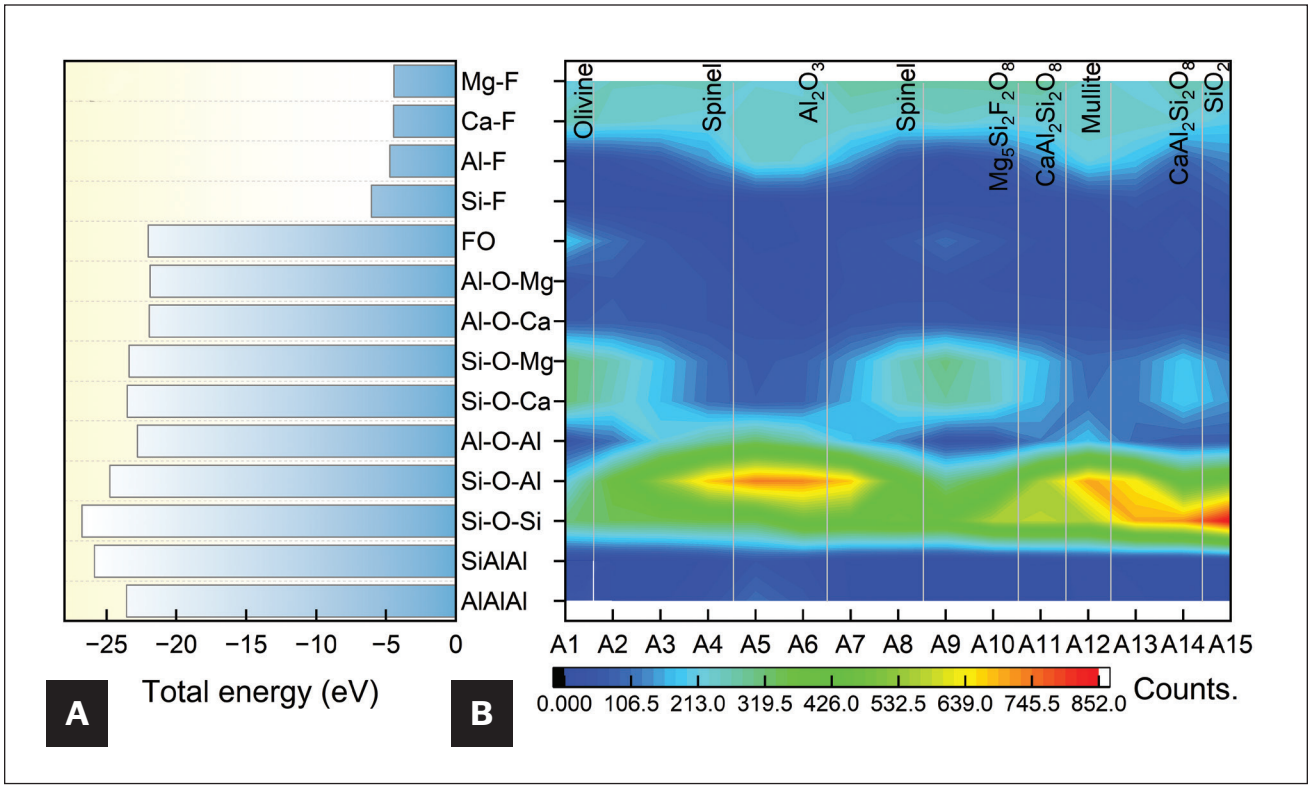

Fig. 7 — A — Total energy of O and F-related bonds; B — bond distribution of targeted systems.

Discussion

Composition and Temperature-Induced Viscosity Variations

SiO_2 content in silicate systems is a key indicator of structural DOP, representing the relative proportion of [SiO_4] tetrahedra. Typically, a higher SiO_2 content corresponds to enhanced structural polymerization (Ref. 32). Higher Al_2O_3/MgO ratios facilitate [AlO_4] tetrahedra formation while impeding active site migration, thus resulting in an increased viscosity. Figure 2 demonstrates the predominant influence of SiO_2 and Al_2O_3 over MgO on viscosity. It is acknowledged that the flux viscosity at 1500°C should be maintained within 0.08–0.3 Pa·s during welding processes (Ref. 33). Consequently, A1 and A9 with low viscosity values may result in inadequate weld pool coverage, whereas excessively high viscosity values observed in A15 could deteriorate the weldability. It is recommended to avoid such extremes when formulating flux compositions. It has been elucidated that incorporating Al_2O_3 into the silicate network generates a substantial amount of Si-O-Al bonds, thereby enhancing the connectivity of the tetrahedral network (Refs. 29, 34). However, such enhancement does not lead to a continuous increase in viscosity. This is attributed to the fact that Al^{3+} ions have a lower valence state than Si^{4+}, which enables some cations to compensate for charge in the network (Ref. 34). As more Al_2O_3 is added, some Al will possess a higher valance state and function as network modifiers, lowering the overall viscosity.

Viscosity always increases as the temperature decreases, as demonstrated in Fig. 2. Thermal vibrations of particles are weakened, which could stabilize large clusters and inhibit viscous flow behaviors (Ref. 35). Subsequently, more solid particles could precipitate as the temperature falls below liquidus. This transition from liquid to heterogeneous system accelerates the increase in viscosity at lower temperatures, especially for A15 (Fig. 2C).

The activation energy for viscous flow (E_η) represents the energy barrier the flow units must overcome to move (Refs. 11, 30). Such parameters can indicate flux fluidity and reflect viscous flow's sensitivity to temperature changes (Refs. 7, 36). This means the temperature-induced viscosity response would be drastic for the liquid with a high E_η value. The relationship between viscosity and temperature can be derived using the Arrhenius equation (Ref. 37):

$$ln\eta = lnA + E_\eta \cdot \frac{1}{RT} \quad (4)$$

where η and T are viscosity and absolute temperature, respectively. A and R are the pre-exponential factor and universal gas constant, respectively.

E_η values are determined by linearly fitting lnη against 1/RT. Fig. 5 illustrates the contour plot of E_η for targeted fluxes. It is observed that E_η peaks at 130.2 kJ/mol in SiO_2-rich regions (A15) and reaches a minimum of 65.40 kJ/mol in MgO-rich regions (A1). This indicates that the atom diffusion rate decreases as more MgO is added, thus improving flux fluidity (Ref. 38), consistent with viscosity measurements in Fig.

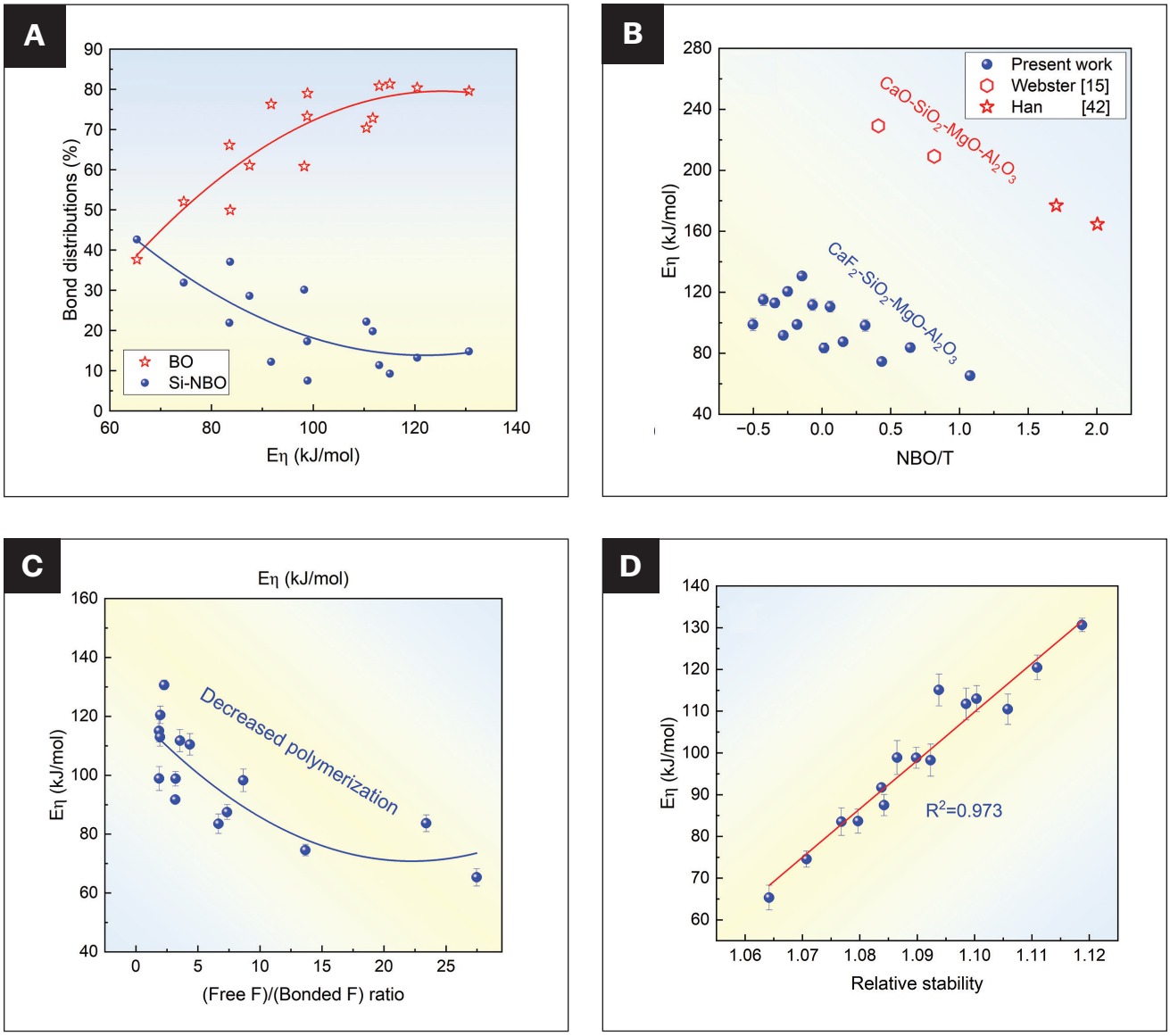

Fig. 8 — Relationship between E_η and structure parameters: A — BO and Si–NBO; B — NBO/T; C — free F/bonded F; D — relative stability (RS).

2. Importantly, the viscosity data selected for E_η calculations fall within the Newtonian fluid range.

Based on the Einstein-Stokes equation, migration behaviors can be described by calculating the self-diffusion coefficients of involved particles. Figure 6 utilizes MD simulations to determine the total diffusion coefficients. The highest diffusion coefficient is observed at A9 (3.07 Å/ns), indicating minimal resistance to flow unit diffusion and, consequently, the least viscosity. This may account for the significantly lowered viscosity of A9 compared to others, with only a slight elevation over A1. However, the lowest diffusion coefficient at A5 (0.160 Å/ns) does not necessarily indicate the highest viscosity, as viscosity may depend on bond stability. Given that Si-O bonds are more stable than Al-O bonds, fluxes abundant in SiO_2 are expected to generate higher viscosity (Ref. 39). The effect of bonds on viscosity will be further explored in subsequent sections.

O/F-Related Bond Structure

Previous studies indicated that a higher proportion of BO correlates with higher DOP and thus higher viscosity (Ref. 40). However, despite A5 having the highest BO and the lowest NBO and FO, its viscosity is lower than that of A15, rich in SiO_2. Therefore, this phenomenon may be related to the presence of F-related structures rather than focusing only on O-related structures. Furthermore, the bond contributions on viscosity need to be further dissected rather than simply categorizing them as BO or NBO, as outlined below.

For the targeted system, fluorine (F) bonding information could enhance our understanding of the relationship between structure and viscosity rather than merely focusing on O-related ones. Figure 4 shows limited F incorporation into [SiO_4] tetrahedral networks and a substantial presence

in [AlO_4] ones. Consequently, it may be inferred that [SiO_4] tetrahedra offers greater stability than [AlO_4] tetrahedra.

As mentioned above, F tends to bond with Ca to form CaF_2 clusters. Notably, the propensity for forming CaF_2 clusters varies with flux compositions. For example, Ca-F bonds are relatively scarce in SiO_2-rich fluxes (31.96%) and markedly more prevalent in MgO-rich fluxes (53.93%). This confirms the closer association between SiO_2 and overall structural stability compared to Al_2O_3, which suggests that F tends to bond with Ca when the overall O-related structure is more stable. Conversely, F readily incorporates into the O-related structure in scenarios with higher MgO content and looser structures. In contrast, A8-A10 fluxes exhibit more Mg-F bonds than A1, which is rich in MgO. Apart from bond distributions, differences in resistance to breakage also contribute to variations in overall viscosity.

Stability and Distribution of Bonds

Bond stability can be quantified through a comprehensive assessment of atomic energy. O atoms are pivotal in silicate networks, wherein lower energy corresponds to greater bond stability (Ref. 13). Consequently, more stable bonds are anticipated to induce enhanced structural stability and, by extension, higher viscosity (Ref. 32). Figure 7 shows detailed bond energy values alongside respective distributions. It is necessary to consider the O-related bond energy, F-related bonds, and corresponding bonding patterns, as the targeted system consists of fluoride and oxides. In Fig. 7A, O-related bonds exhibit lower energies (< −20 eV) compared to F counterparts (> −5 eV), indicating that F-related units are more susceptible to transformation than O-related ones. The Si-O-Si bond emerges with the lowest energy (−26.7391 eV) and epitomizes the greatest thermodynamic stability, consistent with investigations elsewhere (Ref. 41). Conversely, FO and Al-NBO bonds show higher energy values, contributing less to structural polymerization. It is worth noting that the Si-NBO (Si-O-Ca and Si-O-Mg) bond energy is lower than that of the Al-O-Al bond, indicating the superiority of Si-NBO in terms of stability over its Al-O-Al counterpart. This observation demonstrates that relying solely upon the proportion of NBO and BO is inadequate for deriving the overall viscosity.

Figure 7B shows that bonds predominantly consist of BO bonds (Si-O-Si, Si-O-Al, and Al-O-Al) and NBO bonds (Si-O-Ca and Si-O-Mg) for all flux compositions. The bond statistics were obtained by the MATLAB software based on trajectory profiles from MD simulations. A higher DOP is observed under conditions of high SiO_2 + Al_2O_3 contents. Specifically, the proportion of Si-O-Al bonds reach its peak under enriched Al_2O_3 (A5, A6) conditions, indicating the most thorough mixing of [SiO_4] and [AlO_4] structures. The highest proportion of Si-O-Si bonds (A15) correspond to the highest viscosity. As a result, the variation in Si-O-Si bond proportion generates a more consistent correlation with viscosity changes than Si-O-Al bonds.

Figure 7B also annotates corresponding primary phases, calculated by the FactSage software with the Equilib module. The primary phase types can reflect structural DOP, inheriting characteristics from the high-temperature molten structure (Ref. 6). As the composition changes from A1 to A5, Si-O-Si bonds gradually transform into Al-O-Al bonds, thereby transitioning the primary phase from olivine (A1) to spinel (A2-A4) and to corundum (A5). Conversely, as the Al_2O_3 content decreases (A6→A9), the primary phase changes from corundum (A5) to $Mg_5Si_2F_2O_8$ (A9) due to the decrease in Al-related bonds. With continuous additions of SiO_2 and Al_2O_3, the primary phases shift towards those with higher proportions of network formers, corresponding to a gradual increase in viscosity. Previous work shows that the structural unit of primary phase change does result in an abrupt change of activation energy (Ref. 37). This aligns with bond calculations here and the E_η observations for A1 and A15 in Fig. 5, where the structural unit changes (Si-O-Si→Si-O-Al→Al-O-Al) cause drastic E_η variations.

Relationship between Structure Parameters and Viscosity

The bond distributions can be related to viscosity (Ref. 12). The main types in the structure include BO (Si-O-Si, Si-O-Al, and Al-O-Al) and Si–NBO (Si-O-Ca and Si-O-Mg), as depicted in Fig. 7B. Thus, Fig. 8A summarizes the relationship between E_η and the mentioned parameters. It can be observed that there is a positive correlation between E_η and BO. At around 40% BO content, E_η stands at only 60 kJ/mol. However, the E_η value sharply rises to 130 kJ/mol when the BO content exceeds 70%. Conversely, Si–NBO exhibits a negative correlation with E_η and shows a mirror distribution with BO. This suggests that the variations in the proportions of BO and Si–NBO, as primary bond types, can partially reflect the trend in E_η variation.

Considering O-related bonding alone may overlook impacts incurred by CaF_2, constituting 30% of the targeted system. To assess the structural disparities with and without F additions, Fig. 8B illustrates the relationship between NBO/T and E_η alongside the experimental data from CaO-Al_2O_3-SiO_2-MgO (CASM) flux systems (Refs. 15, 42). In both scenarios, an increase in NBO/T correlates with decreased E_η values, indicating lower viscosity with reduced structural polymerization. Substituting CaF_2 for CaO drastically narrows the E_η range from 160–240 kJ/mol to 60–130 kJ/mol, demonstrating that F's impact on O-related structures cannot be ignored. Hence, CaF_2 appears to be an effective agent in reducing flux viscosity.

NBO/T falls short of fully capturing the influence of F in the overall network. Thus, it is imperative to consider F-related bonding information. In the targeted system, F primarily engages in four bonding types: F-Si, F-Al, F-Ca, and F-Mg. Similar to the O classification method, F-Si and F-Al can be regarded as bonded F, while F-Ca and F-Mg are categorized as free F. Therefore, it is suggested that the interaction of F with network formers mimics NBO and thus causes structural depolymerization. However, its association with network modifiers results in free F and dilutes the whole network. Figure 8C illustrates the E_η variation with the ratio of free F to bonded F. An increase in free F promotes a decrease in overall viscosity, with the decreasing trend gradually slowing down. In Fig. 8B, most of the bonded F appears at Al_2O_3-rich regions (A5, A6, and A12) and only depolymerizes the [AlO_4] tetrahedra. However, the free F could simultaneously dilute the [(Si, Al)O_4] tetrahedral structure and is more inclined to decrease the overall viscosity values.

To quantify the bond influence on viscosity, relative stability (RS) is proposed based on the ratio of oxygen energy to

Si-O-Si energy according to Xuan et al. (Equations 5 and 6) (Ref. 13). However, Fig. 7A demonstrates that the energies of F atoms are significantly higher than O ones, which indicates that considering the roles of F atoms is necessary for the targeted system. Hence, the RS calculation could be modified by incorporating the factors associated with F.

$$RS_i = \frac{E_i}{E_{\mathrm{Si-O-Si}}} \tag{5}$$

$$RS = \sum_{i=1}^{m} x_i \cdot RS_i \tag{6}$$

Here, RS_i is the relative stability of the O/F type i, E_i is the average energy of O/F type i, $E_{\mathrm{Si-O-Si}}$ is the energy of O in Si-O-Si bonds, RS is the relative stability of the system, x_i is the content of a specific O/F type, and m is the total number of O/F atoms. Fig. 8D shows the linear fitting results of the E_η and RS values. The E_η increases with an increase in RS values, which matches those observed in earlier studies (Ref. 13). The positive functional relationship between them can be expressed mathematically as Equation 7:

$$E_\eta = 1160 \cdot RS - 1166 \tag{7}$$

Compared with the NBO/T in Fig. 8B, the RS obtained by the MD calculations could demonstrate excellent predictability ($R^2 > 0.97$) of the E_η.

However, it should be mentioned that physical properties such as the interfacial tension and melting temperature can also affect the final welding performance (Refs. 8, 9). Therefore, designing an effective flux requires consideration of multiple physical properties. Future research will further develop a physical properties database and investigate flow behaviors of welding pools under different fluxes.

Conclusions

The correlation between bonds and viscosity of the CaF_2-SiO_2-Al_2O_3-MgO fluxes has been investigated based on experiments and theoretical calculations. Conclusions are obtained as follows.

1. The joint effects of ionic diffusion and bond stability resulted in viscosity fluctuations within the aluminosilicate system, while MgO additions consistently lowered viscosity. The maximum and minimum viscosity values were observed at SiO_2-rich and MgO-rich compositions.

2. Despite having the highest content of BO and TO, Al_2O_3-rich flux does not yield maximum viscosity. This is attributed to the depolymerized [AlO_4] tetrahedra due to bonded F and Al-related bonds' lower bond stability than Si-related ones.

3. CaF_2 significantly decreased E_η because of the dilution effect of free F and the depolymerization effect of bonded F. Therefore, the RS could offer a better method for reflecting the viscosity changes than NBO/T.

Acknowledgments

The authors sincerely acknowledge the financial support from the National Key R&D Program of China (Grant Nos. 2023YFB3709900, 2023YFB3709902, and 2022YFE0123300), the National Natural Science Foundation of China (Grant Nos. U20A20277 and 52350610266) the Fundamental Research Funds for the Central Universities (Grant No. N2402016), and the Major Project of Liaoning Province Innovation Consortium (Grant No. 2023JH1/11200012).

Disclosure Statement

No potential conflict of interest was reported by the author(s).

References

1. Wang, C., and Zhang, J. 2021. Fine-tuning weld metal compositions via flux optimization in submerged arc welding: An overview. *Acta Metallurgica Sinica* 57(9): 1126–1140. DOI: 10.11900/0412.1961.2021.00148

2. Zou, X., Zhao, D., Sun, J., Wang, C., and Matsuura, H. 2017. An integrated study on the evolution of inclusions in EH36 shipbuilding steel with Mg addition: From casting to welding. *Metallurgical and Materials Transactions B* 49(2): 481–489. DOI: 10.1007/s11663-017-1163-x

3. Sengupta, V., Havrylov, D., and Mendez, P. F. 2019. Physical phenomena in the weld zone of submerged arc welding — A review. *Welding Journal* 98: 283-s to 313-s. DOI: 10.29391/2019.98.025

4. Kurlanov, S. A., Potapov, N. N., and Natapov, O. B. 1993. Relationship of physical and welding-technological properties of fluxes for welding low-alloy steels. *Welding International* 7(1): 65–68. DOI: 10.1080/09507119309548346

5. Zhang, J., Wang, C., and Coetsee, T. 2021. Assessment of weld metal compositional prediction models geared towards submerged arc welding: Case studies involving CaF2-SiO_2-MnO and CaO-SiO_2-MnO fluxes. *Metallurgical and Materials Transactions B* 52(4): 2404–2415. DOI: 10.1007/s11663-021-02190-x

6. Yuan, H., Wang, Z., Zhang, Y., Basu, S., Li, Z., and Wang, C. 2024. Uncovering crystallization mechanisms of SiO2–MnO based welding fluxes. *Journal of Non-Crystalline Solids* 627: 122824. DOI: 10.1016/j.jnoncrysol.2024.122824

7. Zhang, Y., Wang, Z., Zhang, J., Li, Z., Basu, S., and Wang, C. 2022. Probing viscosity and structural variations in CaF_2–SiO_2–MnO welding fluxes. *Metallurgical and Materials Transactions B* 53(5): 2814–2823. DOI: 10.1007/s11663-022-02566-7

8. Schwemmer, D. D, Olson, D. L., and Williamson, D L. 1979. The relationship of weld penetration to the welding flux. *Welding Journal* 58(5): 153-s to 160-s.

9. Natalie, C. A., Olson, D. L., and Blander, M. 1986. Physical and chemical behavior of welding fluxes. *Annual Review of Materials Science* 16(1): 389–413. DOI: 10.1146/annurev.ms.16.080186.002133

10. Giordano, D., and Russell, J. K. 2018. Towards a structural model for the viscosity of geological melts. *Earth and Planetary Science Letters* 501: 202–212. DOI: 10.1016/j.epsl.2018.08.031

11. Nakamoto, M., Miyabayashi, Y., Holappa, L., and Tanaka, T. 2007. A model for estimating viscosities of aluminosilicate melts containing alkali oxides. *ISIJ International* 47(10): 1409–1415. DOI: 10.2355/isijinternational.47.1409

12. He, C., Fan, F., Guo, J., Yuan, M., Qin, Y., Wei, Y., and Yan, J. 2024. Viscosity determination of the biomass slag in the SiO2-CaO-K2O system based on the bond distribution. *Fuel* 356: 129642. DOI: 10.1016/j.fuel.2023.129642

13. Xuan, W., Guhl, S., Zhang, Y., Zhang, J., and Meyer, B. 2022. A structural viscosity model for silicate slag melts based on MD simulation. *Ceramics International* 48(19): 28291–28298. DOI: 10.1016/j.ceramint.2022.06.136

14. Yuan, H., Wang, Z., Zhang, Y., and Wang, C. 2023. Roles of MnO and MgO on structural and thermophysical properties of SiO_2-MnO-MgO-B_2O_3 welding fluxes: A molecular dynamics study. *Journal of Molecular Liquids* 386: 122501. DOI: 10.1016/j.molliq.2023.122501

15. Webster, R. I., and Opila, E. J. 2022. Viscosity of CaO-MgO-Al_2O_3-SiO_2 (CMAS) melts: Experimental measurements and comparison to model calculations. *Journal of Non-Crystalline Solids* 584: 121508. DOI: 10.1016/j.jnoncrysol.2022.121508

16. Haghdani, S., Tangstad, M., and Einarsrud, K. E. 2022. A Raman-structure model for the viscosity of SiO_2-CaO-Al_2O_3 system. *Metallurgical and Materials Transactions B* 53(3): 1733–1746. DOI: 10.1007/s11663-022-02483-9

17. Zhang, Y., Coetsee, T., Yang, H., Zhao, T., and Wang, C. 2020. Structural roles of TiO_2 in CaF_2-SiO_2-CaO-TiO_2 submerged arc welding fluxes. *Metallurgical and Materials Transactions B* 51(5): 1947–1952. DOI: 10.1007/s11663-020-01935-4

18. He, S., Wang, S., Jia, B., Li, M., Wang, Q., and Wang, Q. 2019. Molecular dynamics simulation of the structure and properties of CaO-SiO_2-CaF_2 slag systems. *Metallurgical and Materials Transactions B* 50(3): 1503–1513. DOI: 10.1007/s11663-019-01547-7

19. Firoz, S. H., Endo, R., and Susa, M. 2013. Chemical state of fluorine in fluoroaluminosilicate slags in glassy and molten states from perspective of electronic polarisability. *Ironmaking & Steelmaking* 34(5): 437–443. DOI: 10.1179/174328107x168138

20. Zhang, Y., Yuan, H., Tian, H., Wang, Z., and Wang, C. 2023. Elucidating electrical conductive mechanisms for CaF_2–SiO_2–CaO–TiO_2 welding fluxes. *Metallurgical and Materials Transactions B* 54(6): 3023–3030. DOI: 10.1007/s11663-023-02885-3

21. Plimpton, S. 1995. Fast parallel algorithms for short-range molecular dynamics. *Journal of Computational Physics* 117(1): 1–19.

22. Martinez, L., Andrade, R., Birgin, E. G., and Martinez, J. M. 2009. PACKMOL: A package for building initial configurations for molecular dynamics simulations. *Journal of Computational Chemistry* 30(13): 2157–2164. DOI: 10.1002/jcc.21224

23. Bi, Z., Li, K., Jiang, C., Zhang, J., and Ma, S. 2021. Effects of amphoteric oxide (Al_2O_3 and B_2O_3) on the structure and properties of SiO_2-CaO melts by molecular dynamics simulation. *Journal of Non-Crystalline Solids* 559: 120687. DOI: 10.1016/j.jnoncrysol.2021.120687

24. Fan, H., Wang, R., Duan, H., Chen, D., and Xu, Z. 2021. Structural and transport properties of TiO_2-SiO_2-MgO-CaO system through molecular dynamics simulations. *Journal of Molecular Liquids* 325. DOI: 10.1016/j.molliq.2020.115226

25. Wang, Z., Huang, S., Yu, Y., Wen, G., Tang, P., and Hou, Z. 2021. Comprehensive understanding of the microstructure and volatilization mechanism of fluorine in silicate melt. *Chemical Engineering Science* 243: 116773. DOI: 10.1016/j.ces.2021.116773

26. Hennet, L., Drewitt, J. W., Neuville, D. R., Cristiglio, V., Kozaily, J., Brassamin, S., Zanghi, D., and Fischer, H. E. 2016. Neutron diffraction of calcium aluminosilicate glasses and melts. *Journal of Non-Crystalline Solids* 451: 89–93. DOI: 10.1016/j.jnoncrysol.2016.05.018

27. Brown, G., Gibbs, G., and Ribbe, P. 1969. The nature and the variation in length of the Si-O and Al-O bonds in framework silicates. *American Mineralogist* 54(7–8): 1044-1061.

28. Cormier, L., Neuville, D. R., and Calas, G. 2000. Structure and properties of low-silica calcium aluminosilicate glasses. *Journal of Non-Crystalline Solids* 274(1–3): 110-114. DOI: 10.1016/S0022-3093(00)00209-X

29. Gong, K., Özçelik, V. O., Yang, K., and White, C. E. 2021. Density functional modeling and total scattering analysis of the atomic structure of a quaternary CaO-MgO-Al_2O_3-SiO_2 (CMAS) glass: Uncovering the local environment of magnesium. *Physical Review Materials* 5: 015603. DOI: 10.1103/PhysRevMaterials.5.015603

30. Christie, J. K., Pedone, A., Menziani, M. C., and Tilocca, A. 2011. Fluorine environment in bioactive glasses: ab Initio molecular dynamics simulations. *Journal of Physical Chemistry B* 115(9): 2038–2045. DOI: 10.1021/jp110788h

31. Wang, Z., Yu, L., Wen, G., Liu, F., Wang, F., and Barati, M. 2021. A combined computational-experimental study on the effect of Na_2O on the fluoride volatilization in molten slags. *Journal of Molecular Liquids* 342: 117499. DOI: 10.1016/j.molliq.2021.117499

32. Guo, J., He, C., Bai, J., Li, X., and Li, W. 2024. A new viscosity model for the high-iron coal slag based on the bond distribution. *Fuel* 357: 130043. DOI: 10.1016/j.fuel.2023.130043

33. Jackson, C. E. 1960. The science of arc welding. *Welding Journal* 2: 129-s to 140-s.

34. Yang, J., Wang, Z., and Sohn, I. 2022. Topological understanding of thermal conductivity in synthetic slag melts for energy recovery: An experimental and molecular dynamic simulation study. *Acta Materialia* 234: 118014. DOI: 10.1016/j.actamat.2022.118014

35. Kong, L., Bai, J., and Li, W. 2021. Viscosity-temperature property of coal ash slag at the condition of entrained flow gasification: A review. *Fuel Processing Technology* 215: 106751. DOI: 10.1016/j.fuproc.2021.106751

36. Lu, Z., Bai, J., Kong, L., Li, H., Guo, Z., Bai, Z., and Li, W. 2024. Effect of SiO_2/CaO on the viscosity and structure of yellow phosphorus slag in the electric furnace. *Fuel* 358: 130214. DOI: 10.1016/j.fuel.2023.130214

37. Choi, J., Park, T., and Min, D. 2021. Structure-property relationship amphoteric oxide systems via phase stability and ionic structural analysis. *Journal of the American Ceramic Society* 104: 140–156. DOI: 10.1111/jace.17432

38. Zhang, L., Song, X., Wei, J., Yang, J., Lv, P., Su, W., Zhou, Y., and Yu, G. 2023. Simulation and experimental study on the effect of iron on the structure and flow properties of coal ash slag. *Chemical Engineering Science* 273: 118642. DOI: 10.1016/j.ces.2023.118642

39. Wang, Z., and Sohn, I. 2018. Effect of substituting CaO with BaO on the viscosity and structure of CaO-BaO-SiO_2-MgO-Al_2O_3 slags. *Journal of the American Ceramic Society* 101(9): 4285–4296. DOI: 10.1111/jace.15559

40. Mills, K. C., Yuan, L., and Jones, R. T. 2011. Estimating the physical properties of slags. *Journal of the Southern African Institute of Mining and Metallurgy* 111: 649–658.

41. Xuan, W., Yan, S., Zhang, J., Luo, S., Wang, Q., and Zhang, J. 2024. A deep insight into the dynamic crystallization of coal slags and the correlation with melt microstructure. *Fuel Processing Technology* 254: 108005. DOI: 10.1016/j.fuproc.2023.108005

42. Han, C., Chen, M., Zhang, W., Zhao, Z., Evans, T., and Zhao, B. 2016. Evaluation of existing viscosity data and models and developments of new viscosity model for fully liquid slag in the SiO_2-Al_2O_3-CaO-MgO system. *Metallurgical and Materials Transactions B* 47(5): 2861–2874. DOI: 10.1007/s11663-016-0744-4

HANG YUAN, **YANYUN ZHANG**, **HONGYU LIU**, and **CONG WANG** (*wangc@smm.neu.edu.cn*) with Key Laboratory for Ecological Metallurgy of Multimetallic Mineral (Ministry of Education), Northeastern University, Shenyang, Liaoning, China, and School of Metallurgy, Northeastern University, Shenyang, Liaoning, China. **ZUSHU LI** is with WMG, University of Warwick, Coventry, United Kingdom.